Unbiased Filtered Back-Projection in 4π Compton Imaging With 3D Position Sensitive Detectors

Jiyang Chu, Michael Streicher, Jeffrey A. Fessler, *Fellow, IEEE*, and Zhong He, *Senior Member, IEEE*

Abstract—In Compton imaging, iterative methods provide good performance but are usually computationally intensive. Thus, direct inverse algorithms such as filtered back-projection (FBP) are preferable when computation time is limited. The conventional FBP method assumes that the point spread function of a back-projection image is isotropic and invariant to incident direction, as required by frequency spectrum analysis. However, most of the time this assumption is not true because the detector geometry is rarely uniform. Therefore the conventional FBP reconstructed image is biased. To solve the geometry non-uniformity problem, this paper proposes an unbiased FBP algorithm that groups Compton events having the same Compton rings using a system matrix decomposition strategy. The proposed method produces more isotropic resolution, and preserves the capability to use frequency spectrum analysis. The algorithm has been applied to data from a 3D position-sensitive detector array with 4 crystals and a digital readout system. The resulting images had more isotropic resolution than standard FBP.

Index Terms—3D position-sensitive detector, Compton imaging, filtered back-projection, matrix decomposition, unbiased estimation.

I. Introduction

COMPTON imaging uses multi-interaction Compton scattering events to reconstruct radiation distribution images around gamma-ray detectors. Many isotopes emit gamma-ray photons in the range of several hundred keV to several MeV, where Compton scattering dominates the interactions between photons and detector materials. When Compton scattering occurs in a detector, interaction positions and energy depositions are recorded, and scattering angles can be calculated by the Compton formula. Because angular information is provided, the Compton imaging system does not require a mechanical collimator, leading to a simpler system structure and much higher detection efficiency. But the ambiguity of the initial directions on the Compton cone reduces the information of each Compton event, thus some algorithms must be applied to reconstruct the radiation distribution images from the detector observations.

The concept of Compton imaging was initially proposed by Todd, Nightingale and Everett [1], after which different reconstruction algorithms were introduced. As most of the system responses of Compton imagers are very complicated, probability-based iterative algorithms, such as maximum likelihood estimation maximization (MLEM), are widely used [2]–[5]. Because iterative algorithms are usually computationally intensive, researchers continue to investigate direct inverse algorithms, such as filtered back-projection (FBP). FBP has some advantages when real-time imaging is required and computational resources are limited.

Parra [6] applied spherical harmonics (SH) in Compton imaging. The back-projection image in a 4π spherical space is transformed into SH domain, which is a generalized frequency domain, then the deconvolution uses the SH coefficients of an analytical point spread function (PSF). In practice, Xu and He [7] developed a FBP algorithm in a 4π spherical space with SH and a simulated PSF, accounting for the effects of the scattering angle distribution due to the limited detector size. This algorithm is designed for a single cubic CdZnTe detector or similar systems, assuming the PSF changes little for different incident directions. Later Haefner *et al.* [8] proposed another filtering approach that embeds the 4π spherical space in a 3D Cartesian space and uses the 3D Fourier transform and Radon transform. Mathematically this method is equivalent to the SH method with an analytical PSF. All of these FBP methods assume the PSF in back-projection is basically isotropic and invariant to incident direction, which is an acceptable approximation when the influence of detector geometry is not significant. Under this assumption, frequency spectrum analysis can be applied, and filtering can be performed easily.

Currently 3D position sensitive detectors provide advantages for Compton imaging, because a single monolithic detector serves as both the scattering detector and the absorption detector for photons from any incident direction simultaneously, providing higher detection efficiency and intrinsically better 4π imaging capability than traditional dual-plane Compton imagers. In addition the digital readout technique [9], [10] allows sub-pixel position resolution and higher energy resolution, improving the accuracy of image reconstructions. However, with the improvement of angular resolution, the influence of detector geometry on PSF becomes considerable, especially in a detector array with a non-uniform spatial arrangement. As shown in Fig. 1, different incident photon directions have quite different system responses in this 2×2 detector array, leading to a PSF that depends on the incident photon direction. If a fixed PSF is used for FBP, then the

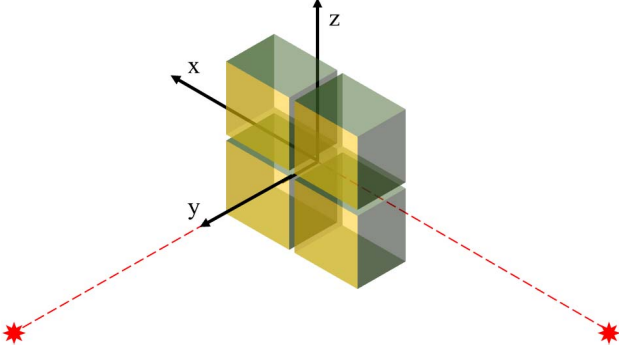Fig. 1. The 2×2 detector array has quite different system responses for different incident photon directions. For a source located on the y-axis, the scattering direction distribution is approximately axisymmetric on the incident direction; but for a source located on the x-axis, with the same scattering angle the scattered photons in the x-z plane have a higher probability of interacting with detectors than the scattered photons in the x-y plane, because the z-dimension of the array is thicker and provides more attenuation than the y-dimension. Therefore, the PSF is not isotropic and varies with incident photon directions.

reconstructed images will have obvious bias because the real PSF never matches the PSF used in reconstruction.

An intuitive solution would be to build PSFs for each incident direction. However, this would require too much computation and loses the capabilities of frequency spectrum analysis. This paper proposes a method based on events grouping and system matrix decomposition, which separates the detector effects from the generalized PSF. With this method the geometric non-uniformity of detectors is considered and the capability of frequency spectrum analysis is preserved. Disregarding noise and discretization effects, an unbiased estimation can be achieved by FBP with a fast spherical harmonics transform. In contrast, references [6] and [8] did not focus on the detector effects but provided algorithms for filtering, and reference [7] incorporated the detector effects into the PSF.

II. FILTERED BACK-PROJECTION

A. Back-Projection and Filtering

In Compton imaging, the source distribution images are usually reconstructed in a 4π spherical space with a far-field assumption. For a given initial energy, a general imaging system can be modeled as:

$$\mathbf{T} \cdot \boldsymbol{f} = \bar{\boldsymbol{g}} \qquad (1)$$

where $\boldsymbol{f}$ is the J-point source distribution image vector to reconstruct, $\bar{\boldsymbol{g}}$ is the expectation of the I-point observation vector $\boldsymbol{g}$, and $\mathbf{T}$ is the system matrix with a size $I \times J$. The elements $\{f_j\}$ of $\boldsymbol{f}$ represent the intensity of different directions/pixels in a 4π spherical space. The elements $\{g_i\}$ of $\boldsymbol{g}$ represent the counts of different event bins. Each event bin is defined as a set of interactions, where each interaction is determined by its 3D position and deposited energy with a binned structure. The elements $\{t_{ij}\}$ of $\mathbf{T}$ are defined as:

$$t_{ij} \triangleq \mathbb{P}(\text{event bin } i \mid \text{photon from direction } j),$$
$$i = 1, 2, \dots, I, \ \ j = 1, 2, \dots, J. \qquad (2)$$

The naive reconstruction algorithm is the simple back-projection (SBP) that simply back-projects the measurements:

$$\hat{\boldsymbol{f}}_{\text{SBP}} = \mathbf{T}' \cdot \boldsymbol{g} \qquad (3)$$

where $\mathbf{T}'$ is the transpose of the system matrix $\mathbf{T}$, $\boldsymbol{g}$ is the real observation vector, and $\hat{\boldsymbol{f}}_{\text{SBP}}$ is the estimated SBP image vector. As this is a linear transform, the expectation of $\hat{\boldsymbol{f}}_{\text{SBP}}$ is:

$$\bar{\boldsymbol{f}}_{\text{SBP}} = \mathbf{T}' \cdot \bar{\boldsymbol{g}} = \mathbf{T}' \cdot \mathbf{T} \cdot \boldsymbol{f} = \mathbf{B} \cdot \boldsymbol{f} \qquad (4)$$

where $\mathbf{B} \triangleq \mathbf{T}' \cdot \mathbf{T}$ is the $J \times J$ point spread matrix of SBP. Mathematically, the jth column of $\mathbf{B}$ is the point spread function of the jth image pixel. Since $\mathbf{B}$ is not an identity matrix, $\hat{\boldsymbol{f}}_{\text{SBP}}$ is a biased estimation of the source distribution image.

To achieve an unbiased estimation, in principle one can apply generalized filtering assuming $\mathbf{B}$ is an invertible matrix:

$$\hat{\boldsymbol{f}}_{\text{FBP}} = \mathbf{B}^{-1} \cdot \hat{\boldsymbol{f}}_{\text{SBP}} = \mathbf{B}^{-1} \cdot \mathbf{T}' \cdot \boldsymbol{g} \qquad (5)$$

where $\hat{\boldsymbol{f}}_{\text{FBP}}$ is the estimated FBP image vector, equivalent to the least square solution of this system model. Again we can get the expectation of $\hat{\boldsymbol{f}}_{\text{FBP}}$:

$$\bar{\boldsymbol{f}}_{\text{FBP}} = \mathbf{B}^{-1} \cdot \bar{\boldsymbol{f}}_{\text{SBP}} = \mathbf{B}^{-1} \cdot \mathbf{B} \cdot \boldsymbol{f} = \boldsymbol{f} \qquad (6)$$

which means $\hat{\boldsymbol{f}}_{\text{FBP}}$ should be an unbiased estimate of the original image $\boldsymbol{f}$. In practice, the inversion in (5) is often very sensitive to noise in $\boldsymbol{g}$ because of small eigenvalues of $\mathbf{B}$, so some form of regularization or apodization is needed. Furthermore, a computationally practical approach to the inversion is preferable, as described next.

B. Matrix-Vector Form of Spherical Harmonics Transform

Calculating the inverse matrix $\mathbf{B}^{-1}$ in (5) would be difficult, especially when the number of image bins and the number of observation bins are very large. Because Compton images are usually reconstructed in a 4π spherical space, eigenvector decomposition using the discrete spherical harmonics transform (DSHT) matrix is a natural choice.

Denote the DSHT matrix as $\mathbf{Q}$. The elements $\{q_{kj}\}$ of $\mathbf{Q}$ are defined as:

$$q_{kj} \triangleq c_j y_{kj}, \ \ k, j = 1, 2, \dots, J \qquad (7)$$

where c_j is the weight of the sampling point f_j, and y_{kj} is defined as:

$$y_{kj} \triangleq Y_l^{m*}(\theta, \phi), \ \ k, j = 1, 2, \dots, J \qquad (8)$$

which are the complex conjugates of the SH functions, $l = 0, 1, \dots, L$, $m = -l, \dots, -1, 0, 1, \dots, l$, and (θ, ϕ) are the sampling directions of image $\boldsymbol{f}$. Ideally the maximum SH degree L satisfies $(L + 1)^2 = K$. Here we have a bijection between the subscript k and the degree-order pair (l, m), as well as a bijection between the subscript j and the polar-azimuth pair (θ, ϕ) at the sampled direction. The complex conjugates of SH are [11]:

$$Y_l^{m*}(\theta, \phi) = \sqrt{\frac{2l + 1}{4\pi} \cdot \frac{(l - m)!}{(l + m)!}} \cdot P_l^m(\cos\theta) e^{-im\phi} \qquad (9)$$

where $P_l^m(\cos\theta)$ are the associated Legendre polynomials.

Define F_{SBP} as the J-point SH coefficients vector of $\hat{f}_{\mathrm{SBP}}$, and F_{FBP} as the J-point SH coefficients vector of $\hat{f}_{\mathrm{FBP}}$, then:

$$F_{\mathrm{SBP}} = \mathbf{Q} \cdot \hat{f}_{\mathrm{SBP}} \Leftrightarrow \hat{f}_{\mathrm{SBP}} = \mathbf{Q}^{-1} \cdot F_{\mathrm{SBP}}, \qquad (10)$$

$$F_{\mathrm{FBP}} = \mathbf{Q} \cdot \hat{f}_{\mathrm{FBP}} \Leftrightarrow \hat{f}_{\mathrm{FBP}} = \mathbf{Q}^{-1} \cdot F_{\mathrm{FBP}}. \qquad (11)$$

Insert (10) and (11) into (5):

$$\mathbf{Q}^{-1} \cdot F_{\mathrm{FBP}} = \mathbf{B}^{-1} \cdot \mathbf{Q}^{-1} \cdot F_{\mathrm{SBP}}, \qquad (12)$$

$$\mathbf{Q} \cdot \mathbf{B} \cdot \mathbf{Q}^{-1} \cdot F_{\mathrm{FBP}} = F_{\mathrm{SBP}}. \qquad (13)$$

Define $\boldsymbol{\Gamma} \triangleq \mathbf{Q} \cdot \mathbf{B} \cdot \mathbf{Q}^{-1}$, which describes the relationship between SBP and FBP in the SH domain:

$$\boldsymbol{\Gamma} \cdot F_{\mathrm{FBP}} = F_{\mathrm{SBP}}. \qquad (14)$$

The DSHT decomposition of the point spread matrix $\mathbf{B}$ is:

$$\mathbf{B} = \mathbf{Q}^{-1} \cdot \boldsymbol{\Gamma} \cdot \mathbf{Q}, \qquad (15)$$

then insert (15) into (5), and the FBP estimation becomes:

$$\hat{f}_{\mathrm{FBP}} = \mathbf{Q}^{-1} \cdot \boldsymbol{\Gamma}^{-1} \cdot \mathbf{Q} \cdot \mathbf{T}' \cdot g. \qquad (16)$$

There exist several fast methods [12]–[16] to compute the DSHT and the inverse DSHT, but we still need to compute another inverse matrix, $\boldsymbol{\Gamma}^{-1}$. An important property is that if the PSF is rotationally invariant in a 4π spherical space, then the point spread matrix $\mathbf{B}$ is diagonalizable with the DSHT matrix, namely $\boldsymbol{\Gamma}$ is a diagonal matrix (see Appendix A for the proof):

$$\boldsymbol{\Gamma} = \mathrm{diag}\{\gamma_j\}, \quad j = 1, 2, \ldots, J \qquad (17)$$

greatly simplifying the computation of $\boldsymbol{\Gamma}^{-1}$. In this case the frequency response of the rotationally invariant point spread function is embedded in the diagonal elements of $\boldsymbol{\Gamma}$, and $\boldsymbol{\Gamma}^{-1}$ works as an inverse filter. To suppress noise, some noise reduction filters can also be incorporated into $\boldsymbol{\Gamma}^{-1}$.

However, most of the time the PSF is not rotationally invariant because of the spatial non-uniformity of the detectors, thus $\boldsymbol{\Gamma}$ is not guaranteed to be diagonal. Traditionally this problem is disregarded and analytical frequency responses or mean frequency responses over all directions are used as the diagonal elements of $\boldsymbol{\Gamma}$, leading to a biased FBP estimation. We describe next a new approach that accommodates detector non-uniformity while still leading to an efficient FBP-type algorithm.

III. SYSTEM MATRIX DECOMPOSITION

A. Conditional Probability Chains

To derive an unbiased and computationally efficient FBP estimator, we need to analyze how the system matrix is generated. To simplify the probability calculation, we assume the incident energy equals the total deposited energy, and the source is monoenergetic in the energy window. Split the probability elements $\{t_{ij}\}$ of $\mathbf{T}$ into conditional probability chains:

$$t_{ij} = \mathbb{P}(I_i^1 \mid D_j) \cdot \mathbb{P}(C_i \mid I_i^1, D_j)$$
$$\cdot \mathbb{P}(E_i^1 \mid C_i, I_i^1, D_j) \cdot \mathbb{P}(I_i^2 \mid E_i^1, C_i, I_i^1, D_j) \qquad (18)$$

where the symbols are defined as:

$$D_j = \{\text{photon from direction } j\},$$
$$I_i^1 = \{\text{first interaction position of event bin } i\},$$
$$C_i = \{\text{scattering direction of event bin } i\},$$
$$E_i^1 = \{\text{first deposited energy of event bin } i\},$$
$$I_i^2 = \{\text{second interaction position of event bin } i\}. \qquad (19)$$

B. Grouped Compton Events

Define $\{\mathbb{S}_k\}$ as the subsets of all Compton event bins, $k = 1, 2, \ldots, K$, where K is the number of all possible Compton rings with binned parameters. The Compton events in the same subset have the same Compton ring, which means they share the same bin of incident energy, the same bin of scattering angle, and the same bin of lever arm direction. Under the far-field assumption, the back-projected rings of these Compton events in the 4π spherical space are the same, but the interaction positions and the distances between two interactions can be different.

Because the initial photon direction will not affect the probability of the second interaction once the first interaction has been determined, we have:

$$\mathbb{P}(I_i^2 \mid E_i^1, C_i, I_i^1, D_j) \equiv \mathbb{P}(I_i^2 \mid E_i^1, C_i, I_i^1) \qquad (20)$$

and denote:

$$\eta_i \triangleq \mathbb{P}(I_i^2 \mid E_i^1, C_i, I_i^1). \qquad (21)$$

In general, η_i is the probability that the scattered photon is absorbed at the second interaction position, which can be calculated from the attenuation process in the detector.

For any i in set $\mathbb{S}_k$, as these events have the same Compton ring, we denote:

$$\psi_{kj} \triangleq \mathbb{P}(E_i^1 \mid C_i, I_i^1, D_j) \qquad (22)$$

in which

$$\mathbb{P}(E_i^1 \mid C_i, I_i^1, D_j) = \begin{cases} 1, & \text{if the Compton formula is satisfied;} \\ 0, & \text{otherwise.} \end{cases} \qquad (23)$$

It is possible to add some uncertainties to blur the Compton ring, but we use the binary form here for simplicity.

For any i in set $\mathbb{S}_k$, as the initial energy and the lever arm direction are determined by the subset $\mathbb{S}_k$, we have that Compton scattering cross section is a constant on the back-projected ring, as shown in Fig. 2, so we define:

$$\sigma_k(j) \triangleq \mathbb{P}(C_i \mid I_i^1, D_j), \qquad (24)$$

$$\sigma_k(j)\psi_{kj} = \begin{cases} \sigma_k, & \text{if the Compton formula is satisfied;} \\ 0, & \text{otherwise.} \end{cases} \qquad (25)$$

Since the incident photons usually have energy exceeding 500 keV for Compton scattering events, they have an approximately uniform probability distribution of interacting with any positions in the detector:

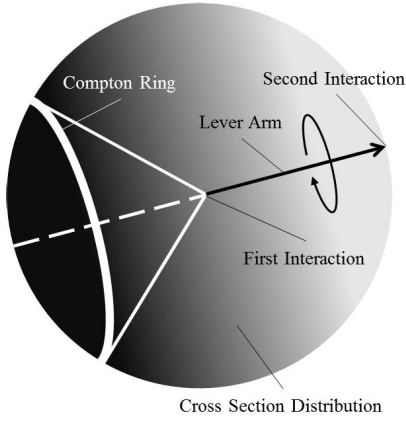$$\mathbb{P}(I_i^1 \mid D_j) \approx \alpha_j. \qquad (26)$$

Fig. 2. For each event in one subset, the incident energy and the lever arm direction of the Compton ring have been determined. By Klein–Nishina formula [17], we know the Compton scattering cross section is a function of incident angles, which is axisymmetric to the lever arm. In the image, darker shading represents a greater cross section, compared to a lighter shading. Given the Compton ring of this subset, the Compton scattering cross section on that ring is a constant value.

This approximation is valid for the detector geometry and type being considered in this paper, and is further analyzed in Appendix B.

Consequently $\forall i \in \mathbb{S}_k$ the conditional probability chains can be written as:

$$t_{ij} = \alpha_j \sigma_k \psi_{kj} \eta_i. \tag{27}$$

To group the probabilities by $\mathbb{S}_k$, denote:

$$s_{kj} \triangleq \sum_{i \in \mathbb{S}_k} t_{ij}, \quad v_k \triangleq \sigma_k \sum_{i \in \mathbb{S}_k} \eta_i, \tag{28}$$

thus from (27) and (28) we get:

$$s_{kj} = \alpha_j \psi_{kj} \cdot \sigma_k \sum_{i \in \mathbb{S}_k} \eta_i = \alpha_j \psi_{kj} v_k = v_k \psi_{kj} \alpha_j. \tag{29}$$

C. System Matrix Decomposition

After grouping the Compton events by the subsets $\{\mathbb{S}_k\}$, we define a new aggregate measurement vector $\boldsymbol{h}$, having elements $\{h_k\}$ of $\boldsymbol{h}$ defined as:

$$h_k \triangleq \sum_{i \in \mathbb{S}_k} g_i, \quad k = 1, 2, \ldots, K. \tag{30}$$

So the system model for the new observation vector is:

$$\mathbf{S} \cdot \boldsymbol{f} = \bar{\boldsymbol{h}} \tag{31}$$

where $\mathbf{S}$ is the new $K \times J$ system matrix with elements $\{s_{kj}\}$, and $\bar{\boldsymbol{h}}$ is the expectation of $\boldsymbol{h}$. Using equation (29), we decompose the system matrix $\mathbf{S}$ as:

$$\mathbf{S} = \mathbf{V} \cdot \boldsymbol{\Psi} \cdot \mathbf{A} \tag{32}$$

where $\boldsymbol{\Psi}$ is a $K \times J$ matrix with elements $\{\psi_{kj}\}$, $\mathbf{A}$ is a $J \times J$ diagonal matrix with elements $\{\alpha_j\}$, and $\mathbf{V}$ is a $K \times K$ diagonal matrix with elements $\{v_k\}$. Now the system model becomes:

$$\mathbf{V} \cdot \boldsymbol{\Psi} \cdot \mathbf{A} \cdot \boldsymbol{f} = \bar{\boldsymbol{h}}. \tag{33}$$

Note that the observation vector $\boldsymbol{h}$ still obeys a Poisson distribution with a mean vector $\bar{\boldsymbol{h}}$. Once we have the system model, we can apply different reconstruction algorithms such as SBP, FBP and MLEM. To show the benefits of the decomposed system matrix, we use $\boldsymbol{\Psi}'$ and $\mathbf{V}$ to do the back-projection:

$$\boldsymbol{\Psi}' \cdot \boldsymbol{\Psi} \cdot \mathbf{A} \cdot \boldsymbol{f} = \boldsymbol{\Psi}' \cdot \mathbf{V}^{-1} \cdot \bar{\boldsymbol{h}} \tag{34}$$

from which we can derive a corrected SBP estimator:

$$\hat{\boldsymbol{f}}_{\text{CSBP}} = \boldsymbol{\Psi}' \cdot \mathbf{V}^{-1} \cdot \boldsymbol{h}. \tag{35}$$

Define the generalized point spread matrix $\tilde{\mathbf{B}}$ as:

$$\tilde{\mathbf{B}} \triangleq \boldsymbol{\Psi}' \cdot \boldsymbol{\Psi} \tag{36}$$

where the jth column is the PSF of the jth pixel. This PSF is the sum of all possible Compton rings intersecting with the incident direction, so $\tilde{\mathbf{B}}$ is rotationally invariant and diagonalizable with the DSHT matrix:

$$\tilde{\mathbf{B}} = \mathbf{Q}^{-1} \cdot \boldsymbol{\Gamma} \cdot \mathbf{Q} \tag{37}$$

in which $\boldsymbol{\Gamma}$ is a diagonal matrix. Finally we have:

$$\boldsymbol{f} = \mathbf{A}^{-1} \cdot \mathbf{Q}^{-1} \cdot \boldsymbol{\Gamma}^{-1} \cdot \mathbf{Q} \cdot \boldsymbol{\Psi}' \cdot \mathbf{V}^{-1} \cdot \bar{\boldsymbol{h}} \tag{38}$$

and the unbiased FBP estimator:

$$\hat{\boldsymbol{f}}_{\text{UFBP}} = \mathbf{A}^{-1} \cdot \mathbf{Q}^{-1} \cdot \boldsymbol{\Gamma}^{-1} \cdot \mathbf{Q} \cdot \boldsymbol{\Psi}' \cdot \mathbf{V}^{-1} \cdot \boldsymbol{h}. \tag{39}$$

Denote the number of Compton events as M, and we know the number of image pixels is J. As $\mathbf{A}^{-1}$, $\boldsymbol{\Gamma}^{-1}$ and $\mathbf{V}^{-1}$ are all diagonal matrices, their multiplications have $O(J)$ time complexity. The DSHT $\mathbf{Q}$ and the inverse DSHT $\mathbf{Q}^{-1}$ both have $O(J^{1.5})$, and the back-projection $\boldsymbol{\Psi}'$ has $O(MJ)$. Since usually $M \gg J$, the unbiased FBP has $O(MJ)$ time complexity, which is as fast as SBP and available for real-time imaging. In addition, one can modify $\boldsymbol{\Gamma}^{-1}$ with some noise reduction filters based on the counting statistics to keep a balance between resolution and variance.

IV. EXPERIMENTS

The experiments used a 2×2 3-dimensional position-sensitive CdZnTe detector array, with 2 mm gaps between crystals. Each crystal in the array was 2 cm $\times$ 2 cm $\times$ 1.5 cm in dimension, and had 11×11 pixels on the 2×2 cm^2 anode surface. With a digital readout technique [9], [10], the detector provides 0.3 mm sub-pixel resolution parallel to the anode surface, 0.3 mm depth resolution perpendicular to the anode surface. With a Cs-137 source, the energy resolution for all double-pixel events is 0.8% FWHM at 662 keV.

The maximum SH degree L used in the DSHT is determined by the intrinsic angular resolution of the imaging system. For our system $L = 60$ was large enough to represent all frequency information. The 4π image space was divided into a 60×120 uniform angular grid. Each sampling point on the grid has a weight based on its corresponding area. The Compton scattering angle was uniformly discretized into 180 bins, thus theoretically the number of subsets $K = 60 \times 120 \times 180 = 1,296,000$ for a given initial energy. Fortunately, as the list-mode data was used in the reconstruction, it was not necessary to calculate all the subsets.
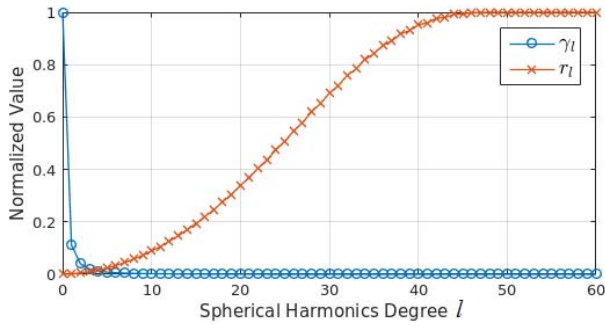
Fig. 3. The filter in the SH domain regards the SH degree l as the frequency. As the frequency response of the PSF is quite small in high frequency area, the direct inverse filter may introduce some high-frequency noise. Thus a DSHT-based Wiener filter was applied to suppress the high frequency components.
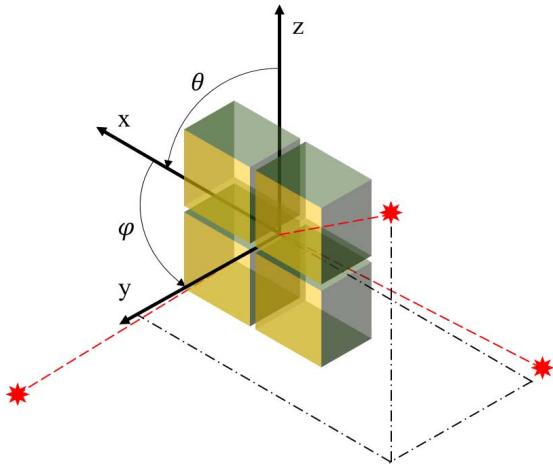

Fig. 4. The Cs-137 source was placed at $(\theta, \phi) = (90°, 92°)$, $(90°, 185°)$, and $(61°, 146°)$ in each measurement. The polar angle θ started from the +z axis, and the azimuth angle ϕ was counter-clockwise from the +x axis direction. The distance between the source and the detector was about 1 m, which was much larger than the size of the detector.

To suppress measurement noise, we applied a DSHT-based Wiener filter in the frequency domain:

$$r_l = \frac{\gamma_l}{\gamma_l^2 + \beta\sigma^2}, \quad l = 1, 2, \ldots, L \tag{40}$$

where $\{\gamma_l\}$ were elements in $\mathbf{\Gamma}$, l were the SH degrees, and the parameter $\beta\sigma^2$ was selected as 10^{-7} empirically. This filter was used for all FBPs in the experiments. The plots of $\{\gamma_l\}$ and $\{r_l\}$ are shown in Fig. 3. In principle, less suppression of high frequencies would improve resolution but amplifies noise. There are many methods about how to choose a noise reduction filter and how to select the hyper-parameters considering the balance between resolution and variance [18]–[25].

A point source was imaged from 3 different directions as shown in Fig. 4. It was a 79 μCi Cs-137 source, and the distance from the source to the detector was 1 m. To limit events to the photo-peak, an energy window of 650-670 keV was used, and we assumed full energy deposition for the summed energy from all interaction sites of a single event. Each measurement lasted 16 hours. The measurements for the sources at $(\theta, \phi) = (90°, 92°)$, $(90°, 185°)$, and $(61°, 146°)$
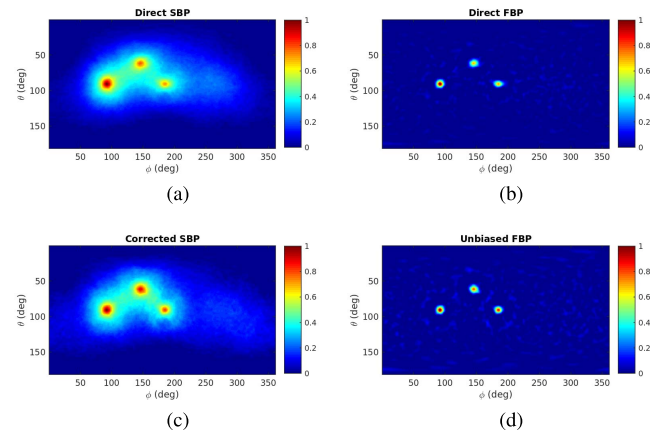

Fig. 5. Three measurements were combined and reconstructed simultaneously. For each position, only 90,000 multi-interaction events were used. (a) In the image of direct SBP, the shapes of hotspots in different positions varied because of the geometric non-uniformity. (b) The direct FBP could improve the FWHM of hotspots. For the hotspot at $(90°, 185°)$ or $(61°, 146°)$, the polar resolution was finer than the azimuth resolution. Thus the hotspot was biased with a non-uniform resolution. (c) With the same data, the hotspots in the corrected SBP became more isotropic. (d) Compared with the direct FBP, the unbiased FBP provided a better performance in FWHM with the same filtering settings. The resolution was nearly uniform along different directions for each hotspot.

generated 276,543 multi-interaction events, 146,256 multi-interaction events, and 95,378 multi-interaction events in the energy window respectively. The detection efficiencies differed due to the geometric non-uniformity. For each measurement, we only used 90,000 multi-interaction events in its reconstruction.

A simple comparison method was applied to decide the sequence of interactions, namely the higher energy interaction was first. In each measurement, we compared the direct methods and the improved methods with the same dataset and filtering settings. The direct methods used analytical system matrix without geometric information of the detector, but the improved methods considered the geometric non-uniformity of the detector.

When the source was placed in front of the cathode side, the PSF in direct SBP was approximately isotropic and the direct filtering approach generated a round hotspot. But when the source was placed at the side of the detector array, the PSF in direct SBP was obviously not isotropic, thus direct filtering would lead to a biased estimation. However, the PSF in corrected SBP showed a rotationally invariant property, and the unbiased FBP was quite stable with different source directions. Fig. 5 shows the reconstruction results where the measurements were combined and reconstructed simultaneously. Fig. 6 shows the comparison between direct filtering approaches and the new filtering approaches with contour images, where each measurement was reconstructed individually.

V. Conclusion

Previously, the conventional FBP for Compton imaging in 4π spherical space assumed that the PSF of the back-projection image was isotropic and invariant to incident
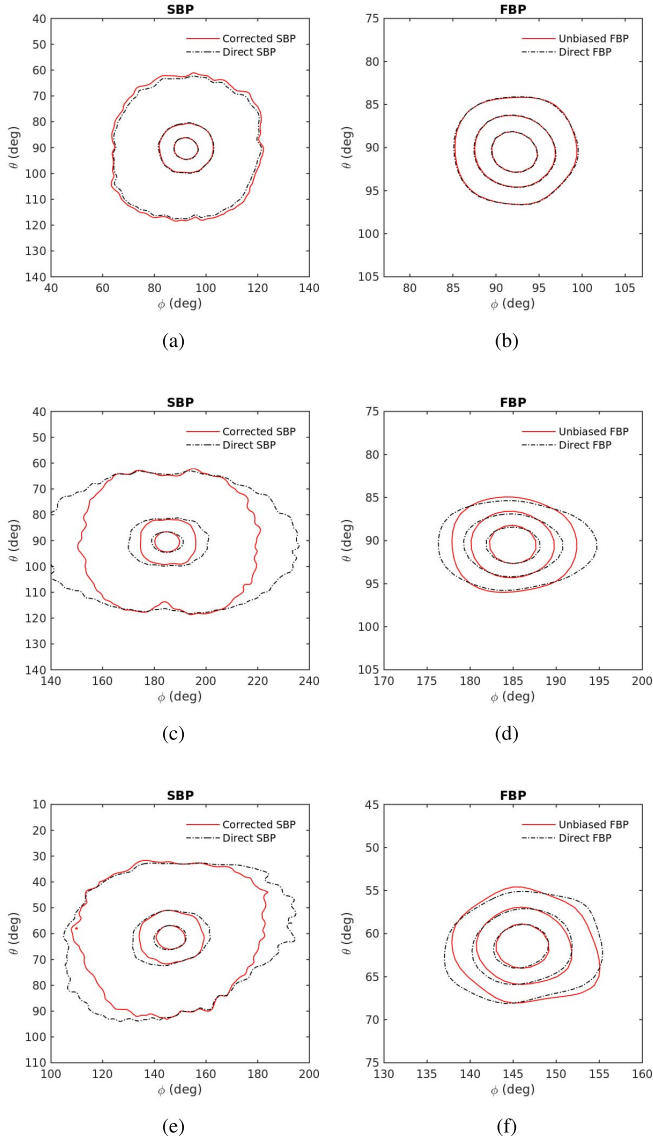
(a)

(b)

(c)

(d)

(e)

(f)

Fig. 6. Each measurement was reconstructed individually. The result of the direct method and the result of the new method were plotted in the same figure for comparison. In each image, the contours from inside to outside indicated 80%, 50%, and 20% of the peak value. Note that the SBP images and the FBP images had different scales. (a)-(b) SBP and FBP images obtained for a source placed at $(90°, 92°)$. The images were all nearly isotropic, and we could not see obvious improvement from new methods. (c)-(d) SBP and FBP images obtained for a source placed at $(90°, 185°)$. In both direct SBP and direct FBP, the impact of geometric non-uniformity is visible as the horizontal elongation of the source. With the same data, the corrected SBP and the unbiased FBP resulted in much more symmetric images and improved azimuthal resolution. (e)-(f) SBP and FBP images obtained for a source placed at $(61°, 146°)$. In both direct SBP and direct FBP, the hotspots tilted to the left because of geometric non-uniformity. With the same data, the corrected SBP and the unbiased FBP resulted in much more symmetric images and improved azimuthal resolution.

directions, because FBP needs frequency spectrum analysis to do fast filtering. However, most of the time this assumption is invalid because the detector geometry is rarely uniform, which means conventional FBP produces biased results without considering the detector geometry. If the PSF is built for each incident angle, the applicability of frequency spectrum analysis will be lost.

To solve this problem, we group the Compton events with the same Compton ring as the same type of events, and build a new system model. By analyzing the conditional probability chains, we decompose the system matrix into several diagonal matrices and a matrix $\mathbf{\Psi}$ made by pure Compton rings. Thus the back-projection with $\mathbf{\Psi}'$ will generate a point spread matrix diagonalizable by the DSHT matrix. Then we get an unbiased FBP estimator, while preserving the capability to use frequency spectrum analysis.

The results obtained with a 2×2 3D position-sensitive CdZnTe detector array show that with the same dataset and filtering settings, the unbiased FBP approach has a more isotropic resolution compared to the direct FBP approach. However, it is noticed that this method increases variance due to different weights of events. The trade-off between unbiased estimation and increased variance is an interesting topic for additional studies. Furthermore, since the observation in the new system model still obeys the Poisson distribution, we can also use it with other reconstruction algorithms such as MLEM, where it could significantly reduce the computational burden since the new matrix is much simpler than the standard one.

APPENDIX I
PROOF OF THE DIAGONALIZABILITY FROM THE ROTATIONALLY INVARIANT POINT SPREAD FUNCTION

Rotational invariance requires the PSF to be isotropic and invariant to incident directions. We denote the rotationally invariant PSF as $b(\cos\omega)$, where ω is the point spread angle between the true incident direction and the calculated incident direction. In a 4π spherical space, denote $f(\mathbf{\Omega})$ as the initial image and $g(\mathbf{\Omega})$ as the image blurred by $b(\cos\omega)$, we have:

$$f(\mathbf{\Omega}) \circledast b(\cos\omega) = g(\mathbf{\Omega}) \tag{41}$$

where $\mathbf{\Omega}$ is the direction, and $\circledast$ represents the convolution in a 4π spherical space. The SH transform pairs of these terms are:

$$f(\mathbf{\Omega}) \overset{\text{SHT}}{\longleftrightarrow} F_l^m,$$
$$g(\mathbf{\Omega}) \overset{\text{SHT}}{\longleftrightarrow} G_l^m,$$
$$b(\cos\omega) \overset{\text{SHT}}{\longleftrightarrow} B_l^0, \tag{42}$$

where F_l^m, G_l^m and B_l^0 are corresponding SH coefficients, and l and m are degrees and orders of the SH coefficients respectively. According to the spherical convolution theorem [12] we have:

$$G_l^m = \sqrt{\frac{4\pi}{2l+1}} B_l^0 \cdot F_l^m. \tag{43}$$

After discretizing and vectorizing, this theorem becomes:

$$\mathbf{B} \cdot \boldsymbol{f} = \boldsymbol{g}, \tag{44}$$
$$\mathbf{\Gamma} \cdot \boldsymbol{F} = \boldsymbol{G}, \tag{45}$$

where $\mathbf{B}$ is the point spread matrix related with $b(\cos\omega)$, $\boldsymbol{F}$ and $\boldsymbol{G}$ are SH coefficients vectors of image vectors $\boldsymbol{f}$ and $\boldsymbol{g}$ respectively, and $\mathbf{\Gamma}$ is the diagonal matrix with the frequency response $\sqrt{4\pi/(2l+1)}B_l^0$ embedded in the diagonal elements. Insert the DSHT equations $\boldsymbol{F} = \mathbf{Q} \cdot \boldsymbol{f}$ and $\boldsymbol{G} = \mathbf{Q} \cdot \boldsymbol{g}$ into (45):

$$\mathbf{\Gamma} \cdot \mathbf{Q} \cdot \boldsymbol{f} = \mathbf{Q} \cdot \boldsymbol{g}, \tag{46}$$

then compare with (44). Considering this equality holds for any initial images f, it is obvious that:

$$\mathbf{B} = \mathbf{Q}^{-1} \cdot \mathbf{\Gamma} \cdot \mathbf{Q} \tag{47}$$

which means the point spread matrix can be diagonalized by the DSHT matrix when the PSF is rotationally invariant.

APPENDIX II
ANALYSIS OF THE FIRST INTERACTION PROBABILITY

Based on the notations in section III, denote $\mathbb{P}(I_i^1 \mid D_j)$ as α_{ij} and we have:

$$\alpha_{ij} = e^{-\mu(E_0)x_{ij}} \cdot p_0(E_0) \tag{48}$$

where E_0 is the initial photon energy, $\mu(E_0)$ is the attenuation coefficient of Compton scattering as a function of E_0, x_{ij} is the distance that the photon from incident angle j penetrates in the detector before the first interaction at position i, and $p_0(E_0)$ is the probability that the photon interacts in a voxel. $p_0(E_0)$ is basically not related with incident angle or interaction position. As $\mu(E_0)x_{ij}$ is usually very small when E_0 is high, we have the approximation:

$$e^{-\mu(E_0)x_{ij}} \approx 1 - \mu(E_0)x_{ij}. \tag{49}$$

If α_j is the average of $\{\alpha_{ij}\}$, then the mean square error (MSE) is:

$$\sqrt{\frac{\sum_i (\alpha_{ij} - \alpha_j)^2}{I}} \approx \mu(E_0)p_0(E_0)\sqrt{\frac{\sum_i (x_{ij} - \bar{x})^2}{I}} \tag{50}$$

where $\bar{x}$ is the average of $\{x_{ij}\}$, and we can find that the MSE is proportional to $\mu(E_0)$. When E_0 is higher, $\mu(E_0)$ is closer to 0 and $\{\alpha_{ij}\}$ are more uniform. Thus it should be a reasonable approximation to replace $\{\alpha_{ij}\}$ by $\{\alpha_j\}$ for Compton scattering events with high initial energy.

REFERENCES

[1] R. W. Todd, J. M. Nightingale, and D. B. Everett, "A proposed γ camera," *Nature*, vol. 251, no. 5471, pp. 132–134, 1974.

[2] S. Wilderman, J. A. Fessler, N. Clinthorne, J. LeBlanc, and W. Rogers, "Improved modeling of system response in list mode EM reconstruction of Compton scatter camera images," *IEEE Trans. Nucl. Sci.*, vol. 48, no. 1, pp. 111–116, Feb. 2001.

[3] C. E. Lehner, Z. He, and F. Zhang, "4π Compton imaging using a 3-D position-sensitive CdZnTe detector via weighted list-mode maximum likelihood," *IEEE Trans. Nucl. Sci.*, vol. 51, no. 4, pp. 1618–1624, Aug. 2004.

[4] D. Xu and Z. He, "Gamma-ray energy-imaging integrated spectral deconvolution," *Nucl. Instrum. Methods Phys. Res. A, Accel. Spectrom. Detect. Assoc. Equip.*, vol. 574, no. 1, pp. 98–109, Apr. 2007.

[5] W. Wang, C. G. Wahl, J. M. Jaworski, and Z. He, "Maximum-likelihood deconvolution in the spatial and spatial-energy domain for events with any number of interactions," *IEEE Trans. Nucl. Sci.*, vol. 59, no. 2, pp. 469–478, Apr. 2012.

[6] L. C. Parra, "Reconstruction of cone-beam projections from Compton scattered data," *IEEE Trans. Nucl. Sci.*, vol. 47, no. 4, pp. 1543–1550, Aug. 2000.

[7] D. Xu and Z. He, "Filtered back-projection in 4π Compton imaging with a single 3D position sensitive CdZnTe detector," *IEEE Trans. Nucl. Sci.*, vol. 53, no. 5, pp. 2787–2796, Oct. 2006.

[8] A. Haefner, D. Gunter, R. Barnowski, and K. Vetter, "A filtered back-projection algorithm for 4π Compton camera data," *IEEE Trans. Nucl. Sci.*, vol. 62, no. 4, pp. 1911–1917, Aug. 2015.

[9] Y. Zhu, S. E. Anderson, and Z. He, "Sub-pixel position sensing for pixelated, 3-D position sensitive, wide band-gap, semiconductor, gamma-ray detectors," *IEEE Trans. Nucl. Sci.*, vol. 58, no. 3, pp. 1400–1409, Jun. 2011.

[10] H. Yang and Z. He, "Identification and reconstruction of single-pixel incomplete charge collection events," *IEEE Trans. Nucl. Sci.*, vol. 60, no. 2, pp. 1243–1247, Apr. 2013.

[11] C. Müller, *Spherical Harmonic*. Berlin, Germany: Springer-Verlag, 1966.

[12] J. Driscoll and D. Healy, "Computing Fourier transforms and convolutions on the 2-sphere," *Adv. Appl. Math.*, vol. 15, no. 2, pp. 202–250, Jun. 1994.

[13] R. Suda and M. Takami, "A fast spherical harmonics transform algorithm," *Math. Comput.*, vol. 71, no. 238, pp. 703–715, Nov. 2001.

[14] S. Kunis and D. Potts, "Fast spherical Fourier algorithms," *J. Comput. Appl. Math.*, vol. 161, no. 1, pp. 75–98, 2003.

[15] M. Reinecke, "Libpsht—Algorithms for efficient spherical harmonic transforms," *Astron. Astrophys.*, vol. 526, Feb. 2011, Art. no. A108.

[16] N. Schaeffer, "Efficient spherical harmonic transforms aimed at pseudospectral numerical simulations," *Geochem. Geophys. Geosyst.*, vol. 14, no. 3, pp. 751–758, Mar. 2013.

[17] O. Klein and Y. Nishina, "Über die streuung von strahlung durch freie elektronen nach der neuen relativistischen quantendynamik von dirac," *Z. Phys.*, vol. 52, no. 11, pp. 853–868, Nov. 1929.

[18] G. Archer and D. M. Titterington, "On some Bayesian/regularization methods for image restoration," *IEEE Trans. Image Process.*, vol. 4, no. 7, pp. 989–995, Jul. 1995.

[19] N. P. Galatsanos and A. K. Katsaggelos, "Methods for choosing the regularization parameter and estimating the noise variance in image restoration and their relation," *IEEE Trans. Image Process.*, vol. 1, no. 3, pp. 322–336, Jul. 1992.

[20] P. Hall and D. M. Titterington, "Common structure of techniques for choosing smoothing parameters in regression problems," *J. Roy. Statist. Soc. B (Methodol.)*, vol. 49, no. 2, pp. 184–198, 1987.

[21] V. E. Johnson, W. H. Wong, X. Hu, and C.-T. Chen, "Image restoration using Gibbs priors: Boundary modeling, treatment of blurring, and selection of hyperparameter," *IEEE Trans. Pattern Anal. Mach. Intell.*, vol. 13, no. 5, pp. 413–425, May 1991.

[22] M. C. Jones, J. S. Marron, and S. J. Sheather, "A brief survey of bandwidth selection for density estimation," *J. Amer. Statist. Assoc.*, vol. 91, no. 433, pp. 401–407, 1996.

[23] M. A. Lukas, "Comparisons of parameter choice methods for regularization with discrete noisy data," *Inverse Problems*, vol. 14, no. 1, p. 161, 1998.

[24] A. M. Thompson, J. C. Brown, J. W. Kay, and D. M. Titterington, "A study of methods of choosing the smoothing parameter in image restoration by regularization," *IEEE Trans. Pattern Anal. Mach. Int.*, vol. 13, no. 4, pp. 326–339, Apr. 1991.

[25] A. M. Thompson and J. Kay, "On some Bayesian choices of regularization parameter in image restoration," *Inverse Problems*, vol. 9, no. 6, p. 749, 1993.